

CCD-3DR: Consistent Conditioning in Diffusion for Single-Image 3D Reconstruction

Yan Di¹, Chenyangguang Zhang², Pengyuan Wang¹, Guangyao Zhai¹, Ruida Zhang², Fabian Manhardt³, Benjamin Busam¹, Xiangyang Ji², and Federico Tombari^{1,3}

¹Technical University of Munich, ²Tsinghua University, ³ Google,

{yan.di@, tombari@in.}tum.de, {zcyg22, zhangrd21}@mails.tsinghua.edu.cn

Abstract

In this paper, we present a novel shape reconstruction method leveraging diffusion model to generate 3D sparse point cloud for the object captured in a single RGB image. Recent methods typically leverage global embedding or local projection-based features as the condition to guide the diffusion model. However, such strategies fail to consistently align the denoised point cloud with the given image, leading to unstable conditioning and inferior performance. In this paper, we present CCD-3DR, which exploits a novel centered diffusion probabilistic model for consistent local feature conditioning. We constrain the noise and sampled point cloud from the diffusion model into a subspace where the point cloud center remains unchanged during the forward diffusion process and reverse process. The stable point cloud center further serves as an anchor to align each point with its corresponding local projection-based features. Extensive experiments on synthetic benchmark ShapeNet-R2N2 demonstrate that CCD-3DR outperforms all competitors by a large margin, with over 40% improvement. We also provide results on real-world dataset Pix3D to thoroughly demonstrate the potential of CCD-3DR in real-world applications. Codes will be released soon.

1. Introduction

Single-image object reconstruction is a well-known ill-posed problem. While deep learning methods have made remarkable strides in achieving high-quality reconstruction, further improvements are still necessary to meet the demands of real-world applications [56, 59]. Recently, a new wave of methods leveraging Denoising Diffusion Probabilistic Model (DDPM) [16] has emerged [3, 27, 31, 32, 38], showcasing superior performance in various domains. For single-image 3D reconstruction with diffusion models, DMPGen [27] and PC² [32] are two representative

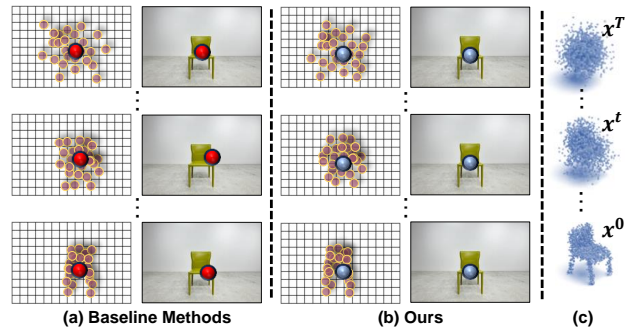


Figure 1. **Baseline Methods vs Ours in Conditioning.** In reverse process (c), the generated point cloud is back-projected onto the feature map of the RGB image and local features are extracted around the projections. Fig (a) and (b) compare the local feature extraction methods of baseline methods [27, 32] and Ours. In (a), during reverse process, the point cloud center gradually deviates (indicated by red points). These deviations result in misaligned feature extraction, leading to a degradation in shape reconstruction quality. In contrast, our method, shown in (b), maintains the projection of the point cloud center unchanged throughout the reverse process (highlighted by blue points), serving as a stable anchor point that facilitates consistent extraction of local features.

baselines. In DMPGen, the condition is the global embedding of the target object, while in PC², in each step of the reverse process, the denoised point cloud is back-projected onto the feature map of the image to extract local feature for each point, which serves as the condition for the next reverse step.

However, directly applying diffusion models in single-image 3D reconstruction suffers from an inevitable challenge: uncontrollable center deviation of the point cloud. Since each point inside the point cloud and predicted noise is independently modelled, under the single-image reconstruction setting, no geometric or contextual priors can be harnessed to control the point cloud center. After each step of the reverse process in DDPM, the gravity center of the generated point cloud will be shifted slightly. Therefore,

from a random sampled Gaussian noise towards the target object, in reverse process, the center of the point cloud will continuously undergo disturbances until it reaches the center of the target object. Based on our experimental findings, we have identified two problems caused by this center deviation.

First, the diffusion network needs to allocate capacity to handle the displacement of the point cloud center. It is crucial to ensure that the transition of the point cloud center from the initial Gaussian noise state to the final object reconstruction is appropriately managed. However, since the overall resource is limited, allocating network capacity to recover the center results in inferior performance in shape reconstruction. **Second**, the center deviation causes misalignment and inconsistency in the local feature conditioning, as used in PC² [32]. The misaligned feature adversely affects the subsequent denoising process in DDPM and degrades the overall quality of the final reconstruction.

To address the aforementioned problems, in this paper, we present CCD-3DR, which takes a single RGB image with corresponding camera pose as input and reconstructs the target object with sparse point cloud. Instead of directly leveraging the off-the-shelf DDPM, we propose a novel Centered denoising Diffusion Probabilistic Model (CDPM) that can enable consistent local feature conditioning in diffusion, which further significantly boosts the single-image reconstruction quality. Our core idea is to constrain the added noise in diffusion process, the predicted noise and sampled point cloud in reverse process into a smaller subspace of the entire sampling space. In this subspace, the center of corresponding noise or point cloud coincides with the origin throughout the diffusion and reverse processes. Thereby, the point cloud center serves as an anchor in local feature extraction to align the point cloud with its corresponding projections consistently.

Based on CDPM, we design CCD-3D for single-image 3D object reconstruction. In CCD-3D, to ensure that the noise and point cloud lie in the subspace defined in CDPM, a straightforward strategy is to iteratively generate samples in the entire space until one sample lie in the subspace. However, this is time-consuming and infeasible in real implementations. We instead first sample in the entire space and then centralize the noise, predicted noise from the diffusion network, denoised point cloud in reverse process to send them to the subspace. We follow PC² [32] to back-project the point cloud onto the feature map of the image to extract local feature around each projection.

In summary, our contributions are listed as follows,

- We propose a novel centered denoising diffusion probabilistic model CDPM, which constrains the noise and point cloud in diffusion and reverse processes into a subspace where the point cloud center is forced to coincide with the origin. CDPM sacrifices some of

DDPM’s generation diversity in exchange for stability in the point cloud center.

- We present a new single-image 3D object reconstruction pipeline CCD-3D, which leverages CDPM to consistently collect local features for the point cloud in diffusion, leading to superior performance in reconstruction quality.
- We evaluate CCD-3D on synthetic dataset ShapeNet-R2N2 to demonstrate its superiority over competitors. CCD-3D outperforms state-of-the-art methods by over 40% under F-Score. Additional experiments on real-world datasets demonstrate the potential of CCD-3D in real applications.

2. Related Works

3D reconstruction of the object shape from a single image has been a research focus in the community [21, 22, 24, 25, 30, 46, 50, 60]. Although being an ill-posed problem, the shape priors in the large-scale training dataset can guide the reconstruction process with generalization ability.

Non-Generative Reconstruction Models. Early methods use 2D encoders [14, 40, 41] to encode features and use 3D decoders [6, 45] to obtain shapes. The pioneering work such as 3D-R2N2 [5] uses the occupancy grids as object shape representations and a following LSTM [17] to fuse inputs from multiple views for prediction. The 2D features are extracted by a 2D CNN and projected to the 3D occupancy grids with a 3D deconvolutional neural network. LSM [21] reprojects 2D features into voxel grids and decode shapes from these grids using a 3D convolutional GRU [4]. Pix2Vox series [52, 53] enjoy a serial architecture composing of a pretrained 2D CNN backbone and 3D transposed convolutional layers with multi-scale fusion to get better voxelized results. Since the voxel representations are limited by the resolution of voxel size, point cloud and mesh-based shape representations are favored to get rid of the limitation [7, 10, 15, 18, 19, 29, 36, 47, 49, 61]. More recent works utilizes implicit representations such as signed distance functions [37, 54], occupancy networks [2, 33] or neural radiance field for object shape generation [20, 48, 57]. Works such as AtlasNet [12] directly generates surface points and reconstructs object meshes, decomposing the problem into the assembly of multiple predicted patches. However, it proves that the auto-encoder architecture has limited generation ability, resulting in less diverse results.

Generative Reconstruction Models. Generative reconstruction models, in contrast to routines mentioned above, estimate the shape distribution in a more explicit way to generate plausible shapes. For the first time to generate point clouds from single-view images, Fan et al. [8] builds a point cloud generation network upon variational autoencoders (VAEs) [23] to generate multiple plausible shapes. By incorporating both VAEs and generative adversarial net-

works (GANs) [11], 3D-VAE-GAN [51] samples latent codes from a single-view image as the condition and outputs 3D shapes through 3D GAN generators. However, It heavily relies on class labels for reconstruction. 3D-aware GANs such as StyleSDF [35] and Get3D [9] can simultaneously synthesize 2D images and 3D detailed meshes. However, these methods suffer from instabilities and mode collapse of GAN training.

Recently, diffusion models [16, 42, 43] exhibit advanced generation ability in such as text-to-image [39], text-to-shape [34] areas, enjoying more stable training phase and elegant mathematical explainability. Thereby, various point cloud related tasks take advantage of diffusion models to get results in higher quality. Luo et al. [27] firstly applies the diffusion process in the point cloud generation task. LION [58] further generalizes the point cloud in the hierarchical latent space with diffusion. Similarly, Lyu et al. [28] utilizes the point diffusion for shape completion. Point-Voxel Diffusion [62] combines multiple representations in the diffusion process to generate stabel results. To get the texture information for the point cloud, [34] generates colored point clouds as the diffusion output for better visualization. Theoretically, such methodology can be readily leveraged into the single-view reconstruction task by regarding the RGB information as the condition [32, 38]. Most recent method PC² [32] projects point clouds in the reverse diffusion process to image plane to query 2D features as shape and color conditions.

3. Method

In the following sections, we outline our methodology. We commence by providing a brief overview of point diffusion models, laying the groundwork for our approach. Subsequently, we elucidate the enhancements we have made to the traditional DDPM, with the intention of augmenting its effectiveness in the realm of single-image reconstruction. These adaptations result in our innovative centered denoising diffusion probabilistic model (CDPM). Lastly, we provide a comprehensive explanation of our single-image reconstruction pipeline CCD-3DR, which is constructed based on CDPM.

3.1. Preliminaries: Diffusion Models

Diffusion denoising probabilistic models are a class of generative models inspired by non-equilibrium thermodynamics. It can iteratively move a set of Gaussian noise towards a uniform and clean point cloud capturing the target object. DDPM contains two Markov chains called the diffusion process and the reverse process. The two processes share a length of $T = 1K$ steps.

Diffusion Process. Let p_0 be the potential distribution of the complete object point cloud x in the dataset and p_T be the standard Gaussian distribution $p_T \sim \mathcal{N}(0_{3N}, I_{3N \times 3N})$,

The diffusion process iteratively adds Gaussian noise ϵ into the clean data distribution p_0 according to the Markov Chain Rule until p_0 reaches p_T . Formally, let $x^0 \sim p_0$, then

$$q(x^{1:T}|x^0) = \prod_{t=1}^T q(x^t|x^{t-1}), \quad (1)$$

$$\text{where } q(x^t|x^{t-1}) = \mathcal{N}(x^t; \sqrt{1 - \beta_t}x^{t-1}, \beta_t \mathbf{I}).$$

The hyperparameter β_t is pre-defined small constants. We use the subscript to denote the diffusion step t . Each $q(x^t|x^{t-1})$ is a Gaussian distribution and $q(x^t|x^0)$ can be reparameterized as,

$$q(x^t|x^0) = \sqrt{\bar{\alpha}_t}x^0 + \epsilon\sqrt{1 - \bar{\alpha}_t}, \quad (2)$$

where $\alpha_t = 1 - \beta_t$, $\bar{\alpha}_t = \prod_{s=0}^t \alpha_s$, and $\epsilon \sim \mathcal{N}(0, \mathbf{I})$.

From Eq. 2, for point diffusion, we can infer that if x^0 is sampled from a zero-mean distribution p_0 , considering ϵ is also zero-mean, $q(x^t|x^0)$ can be modelled as a zero-mean distribution, which mean for any $t \in [0, T]$, the diffusion process will generate a zero-mean distribution at this step. In this paper, we utilize this derivation to boost single-image 3D reconstruction.

Reverse Chain. The reverse process is also a Markov process that removes the noise added in the diffusion process. In this paper, the reverse process is conditioned on the conditioner, an RGB image I capturing the object. We start with a sample $x^T \sim p_T$, and then iteratively sample from $q(x^{t-1}|x^t, f(I))$, where $f(I)$ denotes features extracted from I to incorporate local or global supervision into the reverse process. When the sampling step is sufficiently large (T is large), $q(x^{t-1}|x^t, f(I))$ can be well approximated with an isotropic Gaussian distribution with a fixed small covariance,

$$\begin{aligned} q(x^{t-1}|x^t, f(I)) &= \mathcal{N}(x^{t-1}; \mu_\theta(x^t, f(I)), \sigma_\theta^2 \mathbf{I}), \\ \mu_\theta(x^t, f(I)) &= \frac{1}{\sqrt{\alpha_t}}(x^t - \frac{\beta_t}{\sqrt{1 - \bar{\alpha}_t}}\epsilon_\theta(x^t, f(I))), \end{aligned} \quad (3)$$

where μ_θ is the estimated mean. Thus we can use the network parameterized by θ to directly learn ϵ_θ under the condition $f(I)$.

DDPM-Based Reconstruction Consider a 3D point cloud with N points, DDPM-based reconstruction methods [27, 32] learn a diffusion model $S_\theta : \mathbb{R}^{3N} \rightarrow \mathbb{R}^{3N}$ to denoise the randomly sampled point cloud from p_T into a recognizable object from target distribution p_0 . Specifically, at each step t , the noise is predicted as the offset of each point from the current coordinate in x^t to $x^{t-1} \sim q(x^{t-1}|x^t, f(I))$. Then we sample from $q(x^{t-1}|x^t, f(I))$ to obtain x^{t-1} . As for conditioning, DPMGen [27] encodes the given RGB image into a single global latent vector z and concatenate z with obtained point cloud at each step during

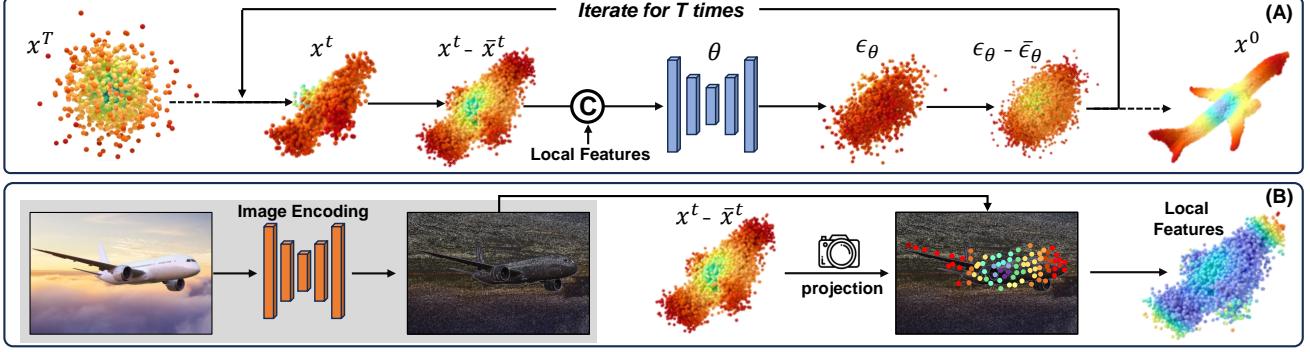


Figure 2. **Architecture of CCD-3D.** Given a single RGB image (capturing the airplane) as the input, CCD-3D aims to reconstruct the object with CDDP. We first leverage a pre-trained MAE [13] model to extract feature maps from the image and interpolate them to the same size as the image (shown in the grey block). The feature maps are utilized to provide local conditions for each point in the denoised point cloud. Block (A) demonstrates the reverse process of CDDP. At step t , point cloud x^t is first centralized to $x^t - \bar{x}^t$ and then concatenated with the local features. The U-Net denoiser θ predicts noise ϵ_θ and centralizes it with $\epsilon_\theta - \bar{\epsilon}_\theta$. The point cloud x^{t-1} can finally be recovered using Eq. 3. Block (B) shows the local feature extraction process. We back-project the centered point cloud $x^t - \bar{x}^t$ onto the image using the given camera pose and collect features around the projections to serve as the local features.

the reverse process. PC² [32] goes one step further by introducing local point-wise features for fine-grained geometry cues. It updates the local feature of each point at each step t by backprojecting the point cloud x^t onto the feature map using the given camera extrinsic $[R_c|T_c]$ and perspective projection matrix π_c ,

$$Proj(x^t) = \pi_c(R_c x^t + T_c). \quad (4)$$

Then local features $f(I)$ around the projections $Proj(x^t)$ are aggregated with rasterization. These two methods [27, 32] are selected as our baselines in this paper.

3.2. Bottlenecks in DDPM Reconstruction

We now analyze the limitations of directly applying DDPM in 3D reconstruction like in DPMGen and PC² [27, 32]. There are two bottlenecks that deteriorate the performance of these methods.

First, predicting the center bias is challenging for the network in the reverse process. Since we assume the variances are constant in all Gaussian distributions, we only need to analyze the center of each denoised point cloud. From x^t to x^{t-1} , in Eq. 1 and 3, we have,

$$E(\bar{x}^{t-1}) = \frac{1}{\sqrt{\alpha_t}} E(\bar{x}^t), \quad E(\bar{\epsilon}_\theta(x^t, f(I))) = 0. \quad (5)$$

Thus after sampling for x^{t-1} , we can obtain,

$$\bar{x}^{t-1} = \frac{1}{\sqrt{\alpha_t}} \left(\bar{x}^t - \frac{\beta_t}{\sqrt{1 - \bar{\alpha}_t}} \bar{\epsilon}_\theta(x^t, f(I)) \right) + \Delta_t, \quad (6)$$

where Δ_t is center bias generated by random sampling from Gaussian distribution for x^{t-1} . When $\bar{x}^T \neq \bar{x}^0$, the network θ needs to move the center of the denoised point cloud

Algorithm 1 CDDP: Training

Repeat:

- 1: $x^0 \sim q(x^0), \quad x^0 = x^0 - \bar{x}^0$
- 2: $t \sim \text{Uniform}(\{1, 2, \dots, T\})$
- 3: $\epsilon \sim \mathcal{N}(\mathbf{0}, \mathbf{I}), \epsilon = \epsilon - \bar{\epsilon}$
- 4: Take gradient descent step on: $\nabla_\theta \|\epsilon - \epsilon_\theta(x^t, f(I))\|^2$

Until converged

from \bar{x}^T towards \bar{x}^0 under the following handicaps. First, $E(\bar{\epsilon}_\theta(x^t, f(I))) = 0$, while the network needs to predict non-zero-mean noise ϵ in several steps to move $\bar{x}^T \rightarrow \bar{x}^0$. Second, the network needs to overcome Δ_t . Last, each point in $x^{T:0}$ is independently modelled in diffusion, and no constraints are incorporated to control the development of the point cloud center. Experiments demonstrate that accurately recovering \bar{x}^0 is a very hard job for the network. And wasting network capacity in recovering center also results in poor performance in shape reconstruction.

Second, the change of the point cloud center makes the local feature conditioning inconsistent. As in PC², the difference Δ_{Proj} in projections of $Proj(\bar{x}^{t-1})$ and $Proj(\bar{x}^t)$ can be derived as

$$\Delta_{Proj} = \pi_c(R_c(\bar{x}^{t-1} - \bar{x}^t) + T_c). \quad (7)$$

If Δ_{Proj} is sufficiently large, the features collected for the point center can be totally different from x^t to x^{t-1} , which will mislead the following denoising steps. Moreover, since we only use single RGB image as conditioner, we have no contextual or geometric constraints to rectify this misalignment.

Algorithm 2 CDPM: Sampling

```
1:  $x^T \sim \mathcal{N}(\mathbf{0}, \mathbf{I}), \quad x^T = x^T - \bar{x}^T$ 
2: for  $t=T, \dots, 1$  do
3:    $\epsilon_\theta = \epsilon_\theta - \bar{\epsilon}_\theta$ 
4:    $x^{t-1} \sim q(x^{t-1}|x^t), x^{t-1} = x^{t-1} - \bar{x}^{t-1}$ 
return  $x^0$ 
```

3.3. From DDPM to CDPM

To address the aforementioned bottlenecks, we propose a novel CDPM model that is designed for single-view 3D reconstruction. The core idea of CDPM is straightforward. To eliminate the influence of center bias in reverse process, we add the following constraint,

$$\bar{x}^t = \mathbf{0}, \quad t = 0, 1, 2, \dots, T. \quad (8)$$

This constraint enforces that the denoised point cloud in each step to be zero-mean, so that the center remains unchanged during the reverse process. As shown in Eq. 2 and Eq. 3, if Eq. 8 holds, we have $\bar{\epsilon} = \mathbf{0}$, $\bar{\epsilon}_\theta(x^t, f(I)) = \mathbf{0}$. Let \mathbb{S}_{x^t} denote the space of all possible samplings from the distribution $q(x^t|x^{t+1})$, then the space under the constraint Eq. 8 $\mathbb{S}_{x^t, \bar{x}^t=\mathbf{0}}$ is a subspace of \mathbb{S}_{x^t} , i.e. $\mathbb{S}_{x^t, \bar{x}^t=\mathbf{0}} \subset \mathbb{S}_{x^t}$. Similarly, we define $\mathbb{S}_\epsilon, \mathbb{S}_{\epsilon, \bar{\epsilon}=\mathbf{0}}, \mathbb{S}_{\epsilon_\theta}, \mathbb{S}_{\epsilon_\theta, \bar{\epsilon}_\theta=\mathbf{0}}$. In summary, from DDPM to CDPM, we constrain $x^t, \epsilon, \epsilon_\theta$ in a smaller subspace,

$$\begin{aligned} \text{DDPM} : x^t \in \mathbb{S}_{x^t}, \epsilon \in \mathbb{S}_\epsilon, \epsilon_\theta \in \mathbb{S}_{\epsilon_\theta} &\implies \\ \text{CDPM} : x^t \in \mathbb{S}_{x^t, \bar{x}^t=\mathbf{0}}, \epsilon \in \mathbb{S}_{\epsilon, \bar{\epsilon}=\mathbf{0}}, \epsilon_\theta \in \mathbb{S}_{\epsilon_\theta, \bar{\epsilon}_\theta=\mathbf{0}}. & \quad (9) \end{aligned}$$

Therefore, we prioritize the stability of the point cloud center to a certain extent, sacrificing a portion of the diversity in diffusion models. For point cloud x^t in reverse process, after obtaining $q(x^t|x^{t+1})$, we can sample multiple times until the sampled point cloud lie in $\mathbb{S}_{x^t, \bar{x}^t=\mathbf{0}}$. However, such strategy is infeasible in real implementation. Thereby we simply first sample in \mathbb{S}_{x^t} and then centralize the point cloud to project it into $\mathbb{S}_{x^t, \bar{x}^t=\mathbf{0}}$, so as to ϵ and ϵ_θ .

Specifically, as explained in Alg. 1 and Alg. 2, we first build a dataset composed of M data pairs $\mathcal{D} = \{(x_i, I_i) | 1 \leq i \leq M\}$, where x_i denotes the i th ground truth point cloud sampled from the object mesh, and I_i is the corresponding RGB image capturing the object. Compared to DDPM, CDPM mainly made improvements in 3 points.

First, the point clouds in \mathcal{D} are centralized as $x_i = x_i - \bar{x}_i$, where \bar{x}_i denotes the gravity center of x_i , establishing a new zero-mean dataset $\bar{\mathcal{D}} = (\bar{x}_i, I_i)$.

Second, for noise ϵ added in diffusion process for training and the noise $\hat{\epsilon}$ predicted in reverse process, we also centralize them as $\epsilon = \epsilon - \bar{\epsilon}$ and $\hat{\epsilon} = \hat{\epsilon} - \bar{\hat{\epsilon}}$, where $\bar{\epsilon}$ and $\bar{\hat{\epsilon}}$ denote the corresponding gravity centers.

Third, during inference, for x^{t-1} sampled from $q(x^{t-1}|x^t, f(I))$, we also centralize x^{t-1} with $x^{t-1} = x^{t-1} - \bar{x}^{t-1}$. From Eq. 2, since we keep x^0 and ϵ to be zero-mean, the diffused point cloud in each step t should be zero-mean.

The advantages of CDPM over DDPM in single-image reconstruction can be summarized as follows.

First, our zero-mean reverse process starts with a zero-mean Gaussian noise and arrives at the zero-mean reconstruction x^0 after T -step zero-mean denoising. This zero-mean nature of the reverse process provides a useful regularization for the network to focus more on the object shape rather than tracking the center of the point cloud. Therefore, our CDPM outperforms the previous DDPM-reconstruction methods even with only global embedding of the object like in [27].

Second, CDPM enables consistent local feature conditioning in the reverse diffusion process. As in PC² [32], the point cloud is back-projected onto the image feature map to extract local point-wise feature as conditioning. However, due to the uncontrollable center bias in reverse process, the projection of each point may gradually deviate, making the local feature aggregation process fail and further deteriorating the final reconstruction quality. In contrast to DDPM-based PC², our method CDPM keeps the gravity center of the denoised point cloud in each step to coincide with the origin, which further serves as an anchor point in local feature collection. The projection of this anchor point remains the same in the reverse process, and thus align the point cloud with the feature map to obtain consistent features.

3.4. CCD-3DR

For fair comparison with baseline methods, we follow PC² [32] to use MAE [13] to extract 2D feature maps from the given RGB image. The feature maps are of equal length and width of the input image to facilitate point cloud projection. For the diffusion network θ used to predict the noise ϵ_θ , we adopt the Point-Voxel CNN (PVCNN) [26]. We use the classic \mathcal{L}_2 loss to supervise the training of θ , as specified in Alg. 1.

4. Experiments

Datasets. We evaluate CCD-3DR on the synthetic dataset ShapeNet-R2N2 [1, 5] and real-world dataset Pix3D [44]. ShapeNet contains a diverse collection of 3D models spanning various object categories, such as furniture, vehicles, and more. The dataset is meticulously annotated, providing not only the 3D geometry of the objects but also rich semantic information, making it an essential tool for quantitative evaluation of single-view reconstruction methods. We follow baseline methods [32, 53, 55] to use the R2N2 [5] subset along with the official image renderings, train-test splits, camera intrinsic and extrinsic matrices. The R2N2

subset covers 13 categories in total. Pix3D [44] is a large-scale benchmark of diverse image-shape pairs with pixel-level 2D-3D alignment. Previous methods [3, 44, 52, 53] only harness the *chair* category and exclude the occluded samples. Since our method needs to use all data to demonstrate robustness towards occlusion, we leverage 3 categories: $\{chair, table, sofa\}$ and randomly generate train-test split with about 90% samples as the training set and the remaining as the testing set. Details are provided in the Supplementary Material.

Implementation Details. We implement CCD-3DR in PyTorch and evaluate the method on a single GeForce RTX 3090Ti GPU with 24GB memory. For ShapeNet-R2N2 [1, 5], we first resize the provided images of size 137×137 to 224×224 and adjust the focal length accordingly. We follow prior work to use 8192 points in training and inference for fairness in computing the F-Score. On Pix3D [44], since the images are of different sizes, we first crop the image with the given bounding box to obtain an object-centric image and then resize it to 224×224 . The camera intrinsic matrix is also adjusted correspondingly. During training, we train CCD-3DR with batch size 16 for 100K steps in total, following PC² [32]. We use the AdamW optimizer with a dynamic learning rate with warmup which increases from 1×10^{-5} to 1×10^{-3} in the first 2K steps, and then decays exponentially until 0 in the following 98K steps.

Baselines. We select DDPM-based DMPGen [27] and PC² [32] as our baseline methods. On ShapeNet-R2N2, we compare with the official results of PC². Since DMPGen doesn't provide results of single-view reconstruction on ShapeNet-R2N2, we reimplement it by using pre-trained MAE [13] to extract global shape code, and then follow the diffusion process in the original paper to reconstruct the object, denoted as DMPGen*. We provide three variants of CCD-3DR on ShapeNet-R2N2, in which *Ours* uses only local features like in PC², *Ours-G* leverages only global features as DMPGen* and *Ours-(G+L)* incorporates both local and global features for reconstruction, as shown in Tab. 5. On Pix3D, we retrain PC² and DMPGen* under the same settings of CCD-3DR.

Evaluation Metrics. We use Chamfer Distance (CD) and F-Score@0.01 [3, 32] as the evaluation metrics. CD quantifies the dissimilarity between two sets of points by measuring the minimum distance from each point in one set to its nearest point in the other set. To compensate the problem that CD can be sensitive to outliers, we also report F-Score with the threshold 0.01, *i.e.*, for each reconstructed point, if its nearest distance to the ground truth point cloud lies below the threshold, it is considered as correctly predicted. Note that previous methods [5, 53, 55] typically report the results using the voxelized 32^3 volume as the shape representation, which quantizes the sampled points and fails to

reflect the reconstruction quality of fine-grained structures. Therefore, we follow PC² [32] to use sampled points from the object mesh as the ground truth. Results of other methods [5, 53, 55] are re-evaluated using the same setting for fair comparisons.

4.1. Comparisons with State-of-the-Art Methods.

Performance on Synthetic Dataset ShapeNet-R2N2. In Tab. 1, we compare CCD-3DR with state-of-the-art competitors on ShapeNet-R2N2 under the F-Score@0.01 metric. 3D-R2N2 [5], Legoforner [55], Pix2vox++ [53] are voxel-based methods, while DMPGen [27], PC² [32] are diffusion-based methods, serving as baselines of CCD-3DR. From Tab. 1, it can be clearly deduced that our method CCD-3DR achieves state-of-the-art performance in 10 out of 13 categories. Considering the *Average* performance, CCD-3DR outperforms previous best method Pix2vox++ with 0.433 *vs.* 0.315, about a 37.5% leap forward. Furthermore, comparing with diffusion-based baseline method PC², CCD-3DR demonstrates superior performance under all the categories, and improves PC² by 40.1%, with 0.433 *vs.* 0.309. We also report the **Oracle** results, following the setting in PC², where for each test image, we predict 5 possible reconstruction results and select the one with highest F-Score@0.01 as the final result. Under the **Oracle** setting, our method surpasses all competitors by a large margin, with about a 20.1% improvement over PC² Oracle.

Performance on Real-World Dataset Pix3D. In Tab. 2 and Tab. 3, we compare CCD-3DR with other DDPM-based reconstruction methods using Chamfer Distance and F-Score@0.01 respectively. Our method consistently outperforms competitors in all categories. On average, CCD-3DR surpasses second-best method PC² by 20% on ShapeNet-R2N2 and 15% on Pix3D.

Qualitative Comparisons. We provide visualization comparisons with previous methods in Fig. 4 and Fig. 3. It can be seen clearly that our method surpasses competitors with respect to the reconstruction quality. Particularly, due to our consistent feature conditioning scheme, our method showcases superiority in recovering fine-grained structures, like the hand in the last row of Tab. 4.

4.2. Ablation Studies

We conduct several ablation studies on the public datasets. Note that except for ablated terms, we leave all other terms and settings unchanged.

Occlusions. In Tab. 4, we evaluate the performance of CCD-3DR with respect to different occlusion ratios on Pix3D. We randomly mask approximately 20% and 50% visible pixels of the object to test the robustness of CCD-3DR towards occlusions. From the table, it can be seen clearly that although the masked pixels increases from 20% to 50%, the performance of CCD-3DR only degrades very

Category	3D-R2N2	LegoFormer	Pix2vox++	DMPGen*	PC ²	Ours	DMPGen*	PC ²	Ours
	[5]	[55]	[53]	[27]	[32]		Oracle	Oracle	Oracle
airplane	0.225	0.215	0.266	0.454	0.473	0.725	0.565	0.681	0.785
bench	0.198	0.241	0.266	0.175	0.305	0.480	0.289	0.444	0.573
cabinet	0.256	0.308	0.317	0.087	0.203	0.282	0.111	0.303	0.371
car	0.211	0.220	0.268	0.310	0.359	0.395	0.402	0.420	0.466
chair	0.194	0.217	0.246	0.171	0.290	0.335	0.312	0.377	0.406
display	0.196	0.261	0.279	0.211	0.232	0.381	0.236	0.357	0.487
lamp	0.186	0.220	0.242	0.207	0.300	0.438	0.347	0.399	0.490
loudspeaker	0.229	0.286	0.297	0.113	0.204	0.219	0.126	0.288	0.291
rifle	0.356	0.364	0.410	0.474	0.522	0.762	0.663	0.686	0.828
sofa	0.208	0.260	0.277	0.078	0.205	0.293	0.106	0.298	0.349
table	0.263	0.305	0.327	0.155	0.270	0.427	0.310	0.420	0.488
telephone	0.407	0.575	0.582	0.333	0.331	0.423	0.464	0.523	0.598
watercraft	0.240	0.283	0.316	0.201	0.324	0.475	0.399	0.424	0.610
Average	0.244	0.289	0.315	0.228	0.309	0.433	0.333	0.432	0.519

Table 1. **Performance on ShapeNet-R2N2.** We compare our method with competitors under F-Score@0.01. The Oracle setting refers to predicting 5 samples of each image and selecting the best prediction as the final result.

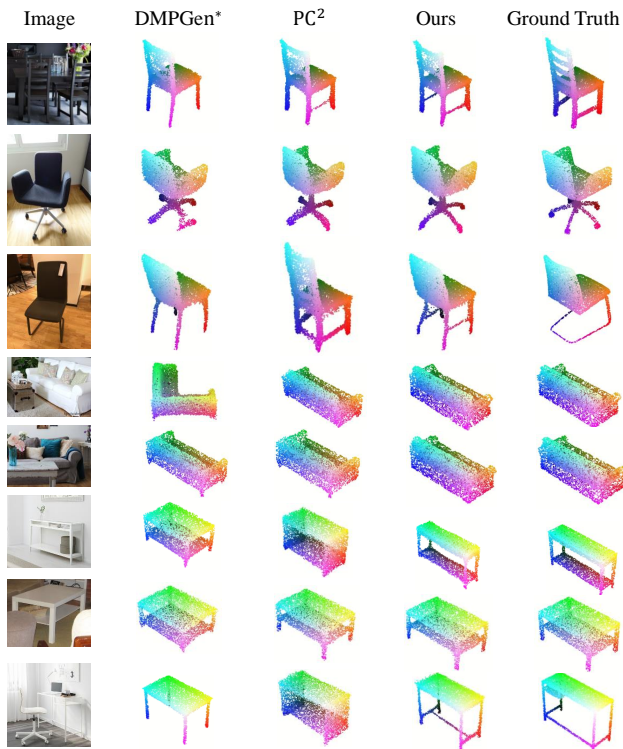


Figure 3. **Qualitative comparisons on real-world dataset Pix3D** [44]. We compare with diffusion-based baseline methods DMPGen* [27] and PC² [32].

little, with 0.013 in *chair*, 0.015 in *table* and 0.024 in *sofa*. Moreover, in this experiment, PC² also demonstrates consistent and satisfactory results under different occlusion ratios, which verifies the capability of diffusion models in handling occlusions. Note that for fair comparisons, we

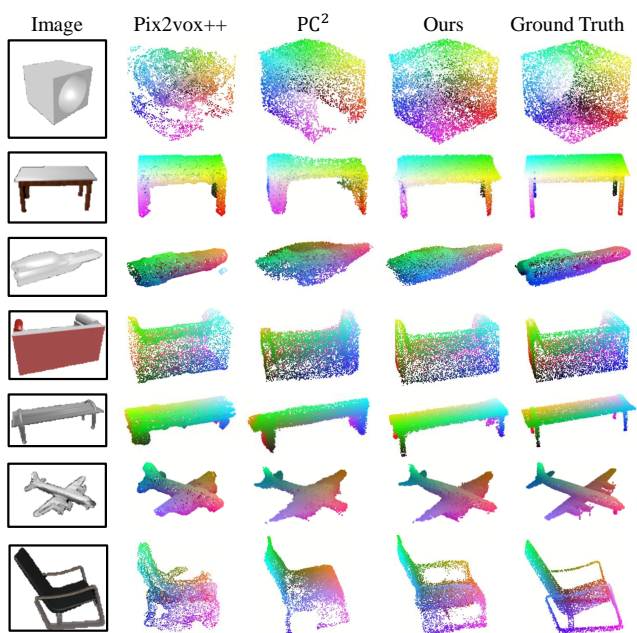


Figure 4. **Qualitative comparisons on synthetic dataset ShapeNet-R2N2** [1, 5]. Our method can recover fine-grained structures accurately, like the handle of the chair.

Method	Chair	Table	Sofa	Average
DMPGen* [27]	0.188	0.176	0.243	0.202
PC ² [32]	0.336	0.294	0.377	0.336
Ours	0.439	0.559	0.489	0.496

Table 2. **Performance on Pix3d.** F-Score@0.01 is reported in the table. Our method outperforms diffusion-based competitors.

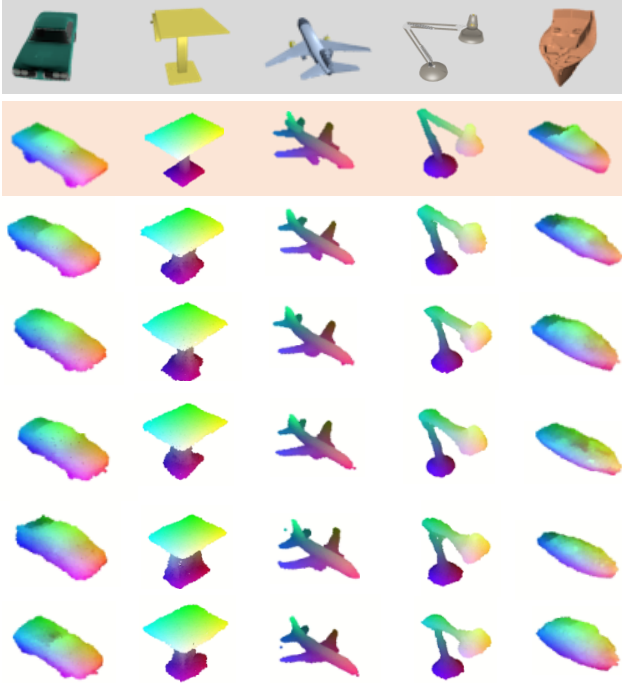


Figure 5. **Visualization of our Oracle results.** The input images and corresponding ground truth shapes are highlighted with grey and orange colors respectively. The 5 reconstruction results are sorted according to the F-Score@0.01 w.r.t the ground truth.

Method	Chair	Table	Sofa	Average
DMPGen* [27]	53.30	50.56	21.04	41.63
PC ² [32]	33.21	13.13	3.760	16.70
Ours	14.98	1.475	0.712	5.722

Table 3. **Performance on Pix3d.** Chamfer Distance ($\times 10^{-3}$) is reported in this table. Our method surpasses baselines by a large margin.

Occ. Ratio	Method	Chair	Table	Sofa
~ 20%	PC ² [32]	0.324	0.280	0.365
	Ours	0.424	0.535	0.421
~ 50%	PC ² [32]	0.310	0.260	0.337
	Ours	0.411	0.520	0.397

Table 4. **Ablation studies of robustness towards occlusions.** Occ. Ratio refers to occlusion ratio. We report the F-Score@0.01 after randomly masking about 20% and 50% visible pixels of the image.

retrain PC² and our method by with the same augmented training data. We randomly mask 0% ~ 50% pixels of each image for training and then conduct the ablation study in Tab. 4.

Local vs. Global Conditioning. In Tab. 5, we demonstrate the effect of local and global features in the diffusion-based reconstruction process. Global feature is obtained by aver-

Category	Ours-G	Ours-(G+L)	Ours
airplane	0.599	0.727	0.725
bench	0.298	0.463	0.480
cabinet	0.204	0.277	0.282
car	0.251	0.398	0.395
chair	0.283	0.341	0.335
display	0.223	0.366	0.381
lamp	0.316	0.429	0.438
loudspeaker	0.177	0.214	0.219
rifle	0.653	0.777	0.762
sofa	0.201	0.287	0.293
table	0.266	0.433	0.427
telephone	0.355	0.414	0.423
watercraft	0.311	0.469	0.475
Average	0.318	0.430	0.433

Table 5. **Ablations on the effect of local and global features on ShapeNet-R2N2.** We retrain and re-evaluate our method using different feature conditioning methods.

aging pooling of the point-wise local features. And when the global feature is incorporated, we directly concatenate it to each point as the condition. Comparing *Ours-(G+L)* and *Ours*, it can be seen clearly that once local feature is provided, additional global feature is not necessary.

Oracle Results. We report the oracle experiment results in Tab. 1. Following the setting in PC², we also predict 5 possible shapes for each image and select the one with highest F-Score@0.01 as the final reconstruction result. It is obvious that under the oracle setting, all the three diffusion-based methods DMPGen*, PC² and Ours showcase a significant leap forward. Thereby, although the centralization scheme in our method may influence the generalization capability of the diffusion model to a certain extent, in the single-view reconstruction case, our method still demonstrate the capability of generating multiple plausible results, as also shown in Fig. 5.

5. Conclusions

In this paper, we propose CCD-3DR, a single-image 3D reconstruction pipeline which leverages a novel centered diffusion probabilistic model for consistent and stable local feature conditioning. We simply project the predicted noise and sampled point cloud from DDPM into a subspace where the point cloud center remains unchanged in the whole diffusion and reverse processes. Extensive experimental results and ablation studies on both synthetic and real-world datasets demonstrate that such a simple design significantly improves the overall performance. We also analyze the influence of point cloud centralization with respect to diversity and point out the limitations of CCD-3DR. In the future, we plan to extend CCD-3DR with an advanced ordinary differential equation solver to enhance the inference speed.

References

- [1] Angel X Chang, Thomas Funkhouser, Leonidas Guibas, Pat Hanrahan, Qixing Huang, Zimo Li, Silvio Savarese, Manolis Savva, Shuran Song, Hao Su, et al. Shapenet: An information-rich 3d model repository. *arXiv preprint arXiv:1512.03012*, 2015. [5](#), [6](#), [7](#)
- [2] Zhiqin Chen and Hao Zhang. Learning implicit fields for generative shape modeling. *2019 IEEE/CVF Conference on Computer Vision and Pattern Recognition (CVPR)*, pages 5932–5941, 2018. [2](#)
- [3] Yen-Chi Cheng, Hsin-Ying Lee, S. Tulyakov, Alexander G. Schwing, and Liangyan Gui. Sdfusion: Multimodal 3d shape completion, reconstruction, and generation. *ArXiv*, abs/2212.04493, 2022. [1](#), [6](#)
- [4] Kyunghyun Cho, Bart van Merriënboer, Caglar Gulcehre, Dzmitry Bahdanau, Fethi Bougares, Holger Schwenk, and Yoshua Bengio. Learning phrase representations using rnn encoder–decoder for statistical machine translation. In *Proceedings of the 2014 Conference on Empirical Methods in Natural Language Processing (EMNLP)*, page 1724. Association for Computational Linguistics, 2014. [2](#)
- [5] Christopher B Choy, Danfei Xu, JunYoung Gwak, Kevin Chen, and Silvio Savarese. 3d-r2n2: A unified approach for single and multi-view 3d object reconstruction. In *Computer Vision–ECCV 2016: 14th European Conference, Amsterdam, The Netherlands, October 11–14, 2016, Proceedings, Part VIII 14*, pages 628–644. Springer, 2016. [2](#), [5](#), [6](#), [7](#)
- [6] Özgün Çiçek, Ahmed Abdulkadir, Soeren S Lienkamp, Thomas Brox, and Olaf Ronneberger. 3d u-net: learning dense volumetric segmentation from sparse annotation. In *Medical Image Computing and Computer-Assisted Intervention–MICCAI 2016: 19th International Conference, Athens, Greece, October 17–21, 2016, Proceedings, Part II 19*, pages 424–432. Springer, 2016. [2](#)
- [7] Philipp Erler, Paul Guerrero, Stefan Ohrhallinger, Niloy Jyoti Mitra, and Michael Wimmer. Points2surf learning implicit surfaces from point clouds. In *European Conference on Computer Vision*, 2020. [2](#)
- [8] Haoqiang Fan, Hao Su, and Leonidas J. Guibas. A point set generation network for 3d object reconstruction from a single image. In *Proceedings of the IEEE Conference on Computer Vision and Pattern Recognition (CVPR)*, July 2017. [2](#)
- [9] Jun Gao, Tianchang Shen, Zian Wang, Wenzheng Chen, K. Yin, Daiqing Li, Or Litany, Zan Gojcic, and Sanja Fidler. Get3d: A generative model of high quality 3d textured shapes learned from images. *ArXiv*, abs/2209.11163, 2022. [3](#)
- [10] Georgia Gkioxari, Jitendra Malik, and Justin Johnson. Mesh r-cnn. *2019 IEEE/CVF International Conference on Computer Vision (ICCV)*, pages 9784–9794, 2019. [2](#)
- [11] Ian Goodfellow, Jean Pouget-Abadie, Mehdi Mirza, Bing Xu, David Warde-Farley, Sherjil Ozair, Aaron Courville, and Yoshua Bengio. Generative adversarial nets. *Advances in neural information processing systems*, 27, 2014. [3](#)
- [12] Thibault Groueix, Matthew Fisher, Vladimir G Kim, Bryan C Russell, and Mathieu Aubry. A papier-mâché approach to learning 3d surface generation. In *Proceedings of the IEEE conference on computer vision and pattern recognition*, pages 216–224, 2018. [2](#)
- [13] Kaiming He, Xinlei Chen, Saining Xie, Yanghao Li, Piotr Dollár, and Ross Girshick. Masked autoencoders are scalable vision learners. In *Proceedings of the IEEE/CVF conference on computer vision and pattern recognition*, pages 16000–16009, 2022. [4](#), [5](#), [6](#)
- [14] Kaiming He, Xiangyu Zhang, Shaoqing Ren, and Jian Sun. Deep residual learning for image recognition. In *Proceedings of the IEEE conference on computer vision and pattern recognition*, pages 770–778, 2016. [2](#)
- [15] Paul Henderson and Vittorio Ferrari. Learning single-image 3d reconstruction by generative modelling of shape, pose and shading. *International Journal of Computer Vision*, 128:835–854, 2019. [2](#)
- [16] Jonathan Ho, Ajay Jain, and Pieter Abbeel. Denoising diffusion probabilistic models. *Advances in neural information processing systems*, 33:6840–6851, 2020. [1](#), [3](#)
- [17] Sepp Hochreiter and Jürgen Schmidhuber. Long short-term memory. *Neural computation*, 9(8):1735–1780, 1997. [2](#)
- [18] T. Hu, Liwei Wang, Xiaogang Xu, Shu Liu, and Jiaya Jia. Self-supervised 3d mesh reconstruction from single images. *2021 IEEE/CVF Conference on Computer Vision and Pattern Recognition (CVPR)*, pages 5998–6007, 2021. [2](#)
- [19] Zixuan Huang, Varun Jampani, Anh Thai, Yuanzhen Li, Stefan Stojanov, and James M. Rehg. Shapeclipper: Scalable 3d shape learning from single-view images via geometric and clip-based consistency. *ArXiv*, abs/2304.06247, 2023. [2](#)
- [20] Won Jun Jang and Lourdes de Agapito. Codenerf: Disentangled neural radiance fields for object categories. *2021 IEEE/CVF International Conference on Computer Vision (ICCV)*, pages 12929–12938, 2021. [2](#)
- [21] Abhishek Kar, Christian Häne, and Jitendra Malik. Learning a multi-view stereo machine. *Advances in neural information processing systems*, 30, 2017. [2](#)
- [22] Abhishek Kar, Shubham Tulsiani, João Carreira, and Jitendra Malik. Category-specific object reconstruction from a single image. *2015 IEEE Conference on Computer Vision and Pattern Recognition (CVPR)*, pages 1966–1974, 2014. [2](#)
- [23] Diederik P Kingma and Max Welling. Auto-encoding variational bayes. *arXiv preprint arXiv:1312.6114*, 2013. [2](#)
- [24] Kejie Li, Ravi Garg, Mingpeng Cai, and Ian D. Reid. Optimizable object reconstruction from a single view. *ArXiv*, abs/1811.11921, 2018. [2](#)
- [25] Kejie Li, Trung T. Pham, Huangying Zhan, and Ian D. Reid. Efficient dense point cloud object reconstruction using deformation vector fields. In *European Conference on Computer Vision*, 2018. [2](#)
- [26] Zhijian Liu, Haotian Tang, Yujun Lin, and Song Han. Point-voxel cnn for efficient 3d deep learning. *Advances in Neural Information Processing Systems*, 32, 2019. [5](#)
- [27] Shitong Luo and Wei Hu. Diffusion probabilistic models for 3d point cloud generation. In *Proceedings of the IEEE/CVF Conference on Computer Vision and Pattern Recognition*, pages 2837–2845, 2021. [1](#), [3](#), [4](#), [5](#), [6](#), [7](#), [8](#)

- [28] Zhaoyang Lyu, Zhifeng Kong, Xudong Xu, Liang Pan, and Dahua Lin. A conditional point diffusion-refinement paradigm for 3d point cloud completion. *ArXiv*, abs/2112.03530, 2021. 3
- [29] Priyanka Mandikal and R. Venkatesh Babu. Dense 3d point cloud reconstruction using a deep pyramid network. *2019 IEEE Winter Conference on Applications of Computer Vision (WACV)*, pages 1052–1060, 2019. 2
- [30] Aihua Mao, Canglan Dai, Qing Liu, Jie Yang, Lin Gao, Ying He, and Yong-Jin Liu. Std-net: Structure-preserving and topology-adaptive deformation network for single-view 3d reconstruction. *IEEE Transactions on Visualization and Computer Graphics*, PP:1–1, 2021. 2
- [31] Luke Melas-Kyriazi, Iro Laina, Christian Rupprecht, and Andrea Vedaldi. Realfusion: 360deg reconstruction of any object from a single image. In *Proceedings of the IEEE/CVF Conference on Computer Vision and Pattern Recognition*, pages 8446–8455, 2023. 1
- [32] Luke Melas-Kyriazi, Christian Rupprecht, and Andrea Vedaldi. Pc2: Projection-conditioned point cloud diffusion for single-image 3d reconstruction. In *Proceedings of the IEEE/CVF Conference on Computer Vision and Pattern Recognition*, pages 12923–12932, 2023. 1, 2, 3, 4, 5, 6, 7, 8
- [33] Lars M. Mescheder, Michael Oechsle, Michael Niemeyer, Sebastian Nowozin, and Andreas Geiger. Occupancy networks: Learning 3d reconstruction in function space. *2019 IEEE/CVF Conference on Computer Vision and Pattern Recognition (CVPR)*, pages 4455–4465, 2018. 2
- [34] Alex Nichol, Heewoo Jun, Pratul D. Dhariwal, Pamela Mishkin, and Mark Chen. Point-e: A system for generating 3d point clouds from complex prompts. *ArXiv*, abs/2212.08751, 2022. 3
- [35] Roy Or-El, Xuan Luo, Mengyi Shan, Eli Shechtman, Jeong Joon Park, and Ira Kemelmacher-Shlizerman. Stylesdf: High-resolution 3d-consistent image and geometry generation. *2022 IEEE/CVF Conference on Computer Vision and Pattern Recognition (CVPR)*, pages 13493–13503, 2021. 3
- [36] Junyi Pan, Xiaoguang Han, Weikai Chen, Jiapeng Tang, and Kui Jia. Deep mesh reconstruction from single rgb images via topology modification networks. *2019 IEEE/CVF International Conference on Computer Vision (ICCV)*, pages 9963–9972, 2019. 2
- [37] Jeong Joon Park, Peter R. Florence, Julian Straub, Richard A. Newcombe, and S. Lovegrove. Deepsdf: Learning continuous signed distance functions for shape representation. *2019 IEEE/CVF Conference on Computer Vision and Pattern Recognition (CVPR)*, pages 165–174, 2019. 2
- [38] Ben Poole, Ajay Jain, Jonathan T Barron, and Ben Mildenhall. Dreamfusion: Text-to-3d using 2d diffusion. *arXiv preprint arXiv:2209.14988*, 2022. 1, 3
- [39] Robin Rombach, A. Blattmann, Dominik Lorenz, Patrick Esser, and Björn Ommer. High-resolution image synthesis with latent diffusion models. *2022 IEEE/CVF Conference on Computer Vision and Pattern Recognition (CVPR)*, pages 10674–10685, 2021. 3
- [40] Olaf Ronneberger, Philipp Fischer, and Thomas Brox. U-net: Convolutional networks for biomedical image segmentation. In *Medical Image Computing and Computer-Assisted Intervention—MICCAI 2015: 18th International Conference, Munich, Germany, October 5-9, 2015, Proceedings, Part III 18*, pages 234–241. Springer, 2015. 2
- [41] Karen Simonyan and Andrew Zisserman. Very deep convolutional networks for large-scale image recognition. *arXiv preprint arXiv:1409.1556*, 2014. 2
- [42] Yang Song and Stefano Ermon. Generative modeling by estimating gradients of the data distribution. *Advances in neural information processing systems*, 32, 2019. 3
- [43] Yang Song and Stefano Ermon. Improved techniques for training score-based generative models. *Advances in neural information processing systems*, 33:12438–12448, 2020. 3
- [44] Xingyuan Sun, Jiajun Wu, Xiuming Zhang, Zhoutong Zhang, Chengkai Zhang, Tianfan Xue, Joshua B Tenenbaum, and William T Freeman. Pix3d: Dataset and methods for single-image 3d shape modeling. In *Proceedings of the IEEE conference on computer vision and pattern recognition*, pages 2974–2983, 2018. 5, 6, 7
- [45] Du Tran, Lubomir Bourdev, Rob Fergus, Lorenzo Torresani, and Manohar Paluri. Learning spatiotemporal features with 3d convolutional networks. In *Proceedings of the IEEE international conference on computer vision*, pages 4489–4497, 2015. 2
- [46] Nanyang Wang, Yinda Zhang, Zhuwen Li, Yanwei Fu, W. Liu, and Yu-Gang Jiang. Pixel2mesh: Generating 3d mesh models from single rgb images. In *European Conference on Computer Vision*, 2018. 2
- [47] Nanyang Wang, Yinda Zhang, Zhuwen Li, Yanwei Fu, Hang Yu, Wei Liu, X. Xue, and Yu-Gang Jiang. Pixel2mesh: 3d mesh model generation via image guided deformation. *IEEE Transactions on Pattern Analysis and Machine Intelligence*, 43:3600–3613, 2020. 2
- [48] Peng Wang, Lingjie Liu, Yuan Liu, Christian Theobalt, Taku Komura, and Wenping Wang. Neus: Learning neural implicit surfaces by volume rendering for multi-view reconstruction. In *Neural Information Processing Systems*, 2021. 2
- [49] Chao Wen, Yinda Zhang, Zhuwen Li, and Yanwei Fu. Pixel2mesh++: Multi-view 3d mesh generation via deformation. *2019 IEEE/CVF International Conference on Computer Vision (ICCV)*, pages 1042–1051, 2019. 2
- [50] Jiajun Wu, Yifan Wang, Tianfan Xue, Xingyuan Sun, Bill Freeman, and Joshua B. Tenenbaum. Marnet: 3d shape reconstruction via 2.5d sketches. In *NIPS*, 2017. 2
- [51] Jiajun Wu, Chengkai Zhang, Tianfan Xue, Bill Freeman, and Joshua B. Tenenbaum. Learning a probabilistic latent space of object shapes via 3d generative-adversarial modeling. In *NIPS*, 2016. 3
- [52] Haozhe Xie, Hongxun Yao, Xiaoshuai Sun, Shangchen Zhou, and Shengping Zhang. Pix2vox: Context-aware 3d reconstruction from single and multi-view images. In *Proceedings of the IEEE/CVF international conference on computer vision*, pages 2690–2698, 2019. 2, 6
- [53] Haozhe Xie, Hongxun Yao, Shengping Zhang, Shangchen Zhou, and Wenxiu Sun. Pix2vox++: Multi-scale context-aware 3d object reconstruction from single and multiple images. *International Journal of Computer Vision*, 128(12):2919–2935, 2020. 2, 5, 6, 7

- [54] Qiangeng Xu, Weiyue Wang, Duygu Ceylan, Radomír Mech, and Ulrich Neumann. Disn: Deep implicit surface network for high-quality single-view 3d reconstruction. *ArXiv*, abs/1905.10711, 2019. [2](#)
- [55] Farid Yagubbayli, Yida Wang, Alessio Tonioni, and Federico Tombari. Legoforner: Transformers for block-by-block multi-view 3d reconstruction. *arXiv preprint arXiv:2106.12102*, 2021. [5](#), [6](#), [7](#)
- [56] Shichao Yang and Sebastian Scherer. Cubeslam: Monocular 3-d object slam. *IEEE Transactions on Robotics*, 35(4):925–938, 2019. [1](#)
- [57] Alex Yu, Vickie Ye, Matthew Tancik, and Angjoo Kanazawa. pixelnerf: Neural radiance fields from one or few images. *2021 IEEE/CVF Conference on Computer Vision and Pattern Recognition (CVPR)*, pages 4576–4585, 2020. [2](#)
- [58] Xiaohui Zeng, Arash Vahdat, Francis Williams, Zan Gojcic, Or Litany, Sanja Fidler, and Karsten Kreis. Lion: Latent point diffusion models for 3d shape generation. *ArXiv*, abs/2210.06978, 2022. [3](#)
- [59] Guangyao Zhai, Dianyue Huang, Shun-Cheng Wu, HyunJun Jung, Yan Di, Fabian Manhardt, Federico Tombari, Nassir Navab, and Benjamin Busam. Monograspnet: 6-dof grasping with a single rgb image. In *2023 IEEE International Conference on Robotics and Automation (ICRA)*, pages 1708–1714. IEEE, 2023. [1](#)
- [60] Xuancheng Zhang, Rui Ma, Changqing Zou, Minghao Zhang, Xibin Zhao, and Yue Gao. View-aware geometry-structure joint learning for single-view 3d shape reconstruction. *IEEE Transactions on Pattern Analysis and Machine Intelligence*, 44:6546–6561, 2021. [2](#)
- [61] Xiuming Zhang, Zhoutong Zhang, Chengkai Zhang, Joshua B. Tenenbaum, Bill Freeman, and Jiajun Wu. Learning to reconstruct shapes from unseen classes. *ArXiv*, abs/1812.11166, 2018. [2](#)
- [62] Linqi Zhou, Yilun Du, and Jiajun Wu. 3d shape generation and completion through point-voxel diffusion. In *Proceedings of the IEEE/CVF International Conference on Computer Vision (ICCV)*, pages 5826–5835, October 2021. [3](#)